Eddy properties in the California Current System

Jaison Kurian,[1] Francois Colas,[1] Xavier Capet,[2] James C. McWilliams,[1] and Dudley B. Chelton[3]

Received 16 December 2010; revised 24 March 2011; accepted 20 May 2011; published 25 August 2011.

[1] Eddy detection and tracking algorithms are applied to both satellite altimetry and a high-resolution (dx = 5 km) climatological model solution of the U.S. West Coast to study the properties of surface and undercurrent eddies in the California Current System. Eddy properties show remarkable similarity in space and time, and even somewhat in polarity. Summer and fall are the most active seasons for undercurrent eddy generation, while there is less seasonal variation at surface. Most of the eddies have radii in the range of 25–100 km, sea level anomaly amplitudes of 1–4 cm, and vorticity normalized by f amplitudes of 0.025–0.2. Many of the eddies formed near the coast travel considerable distance westward with speeds about 2 km/day, consistent with the β effect. Anticyclones and cyclones show equatorward and poleward displacements, respectively. Long-lived surface eddies show a cyclonic dominance. The subsurface California Undercurrent generates more long-lived anticyclones than cyclones through instabilities and topographic/coastline effects. In contrast, surface eddies and subsurface cyclones have much more widely distributed birth sites. The majority of the identified eddies have lifetimes less than a season. Eddies extend to 800–1500 m depth and have distinctive vertical structures for cyclones and anticyclones. Eddies show high nonlinearity (rotation speed higher than propagation speed) and hence can be efficient in transporting materials offshore.

Citation: Kurian, J., F. Colas, X. Capet, J. C. McWilliams, and D. B. Chelton (2011), Eddy properties in the California Current System, *J. Geophys. Res.*, *116*, C08027, doi:10.1029/2010JC006895.

1. Introduction

[2] The California Current System (CCS) is one of the most productive and well-studied eastern boundary upwelling systems. It is a region of high mesoscale activity, with frequent formation of eddies, fronts, and filaments throughout the year, as evident from the satellite altimetry [*Kelly et al.*, 1998; *Strub and James*, 2000], drifter observations [*Garfield et al.*, 1999] and numerical simulations [*Marchesiello et al.*, 2003]. An important aspect of the CCS is the numerous mesoscale eddies generated by surface and subsurface currents, which influence the circulation, transport, and mixing in this region. In addition, they also have significant impact on the ecosystem through offshore transport of nutrients from the coast and injection of subsurface nutrients into the euphotic zone [*Logerwell and Smith*, 2001; *Mantyla et al.*, 2008].

[3] The CCS is characterized by a broad (~1000 km) and shallow (upper 300 m) equatorward California Current (CC) at the surface and a narrow (100 km from the coast), poleward California Undercurrent over the continental slope at the subsurface (100–400 m) [*Hickey*, 1979; *Chelton*, 1984; *Hickey*, 1998; *Collins et al.*, 2000; *Pierce et al.*, 2000] (Figure 1). A weak (~5 cm/s) inshore poleward current, the Davidson Current, exists near the coast north of Point Conception during fall and winter. The CC is relatively slow (~10–30 cm/s) and carries fresh cool water of northern origin to the south at the surface. The undercurrent carries relatively warm, salty, and oxygen-poor water of equatorial origin to the north [*Hickey*, 1979]. Though the undercurrent exists throughout the year, summer and fall are the seasons for its maximum speed, reaching about 8 cm/s [*Lynn and Simpson*, 1987; *Pierce et al.*, 2000] (Figure 1). Instabilities in these currents create energetic mesoscale eddies [*Batteen et al.*, 2003; *Marchesiello et al.*, 2003; *Capet et al.*, 2008; M. J. Molemaker, Submesoscale generation of mesoscale anticyclones in the California Undercurrent, submitted to *Journal of Physical Oceanography*, 2010] (Figure 1). Wind forcing is also considered to be important for eddy generation, especially at the surface [*Pares-Sierra et al.*, 1993].

[4] Properties of the CCS mesoscale eddies are mainly known from individual field observations or floats deployed at specific locations during specific times. Perhaps the most interesting aspect that emerged from the observations is that eddies generated by the CC at the surface are predominantly cyclones with a surface core (in the upper 150 m), whereas those spawned by the undercurrent at subsurface are mainly

[1]Institute of Geophysics and Planetary Physics, University of California, Los Angeles, California, USA.
[2]Laboratoire de Physique des Océans, UMR 6523, CNRS-IFREMER-UBO, Plouzane, France.
[3]College of Oceanic and Atmospheric Sciences, Oregon State University, Corvallis, Oregon, USA.

0148-0227/11/2010JC006895

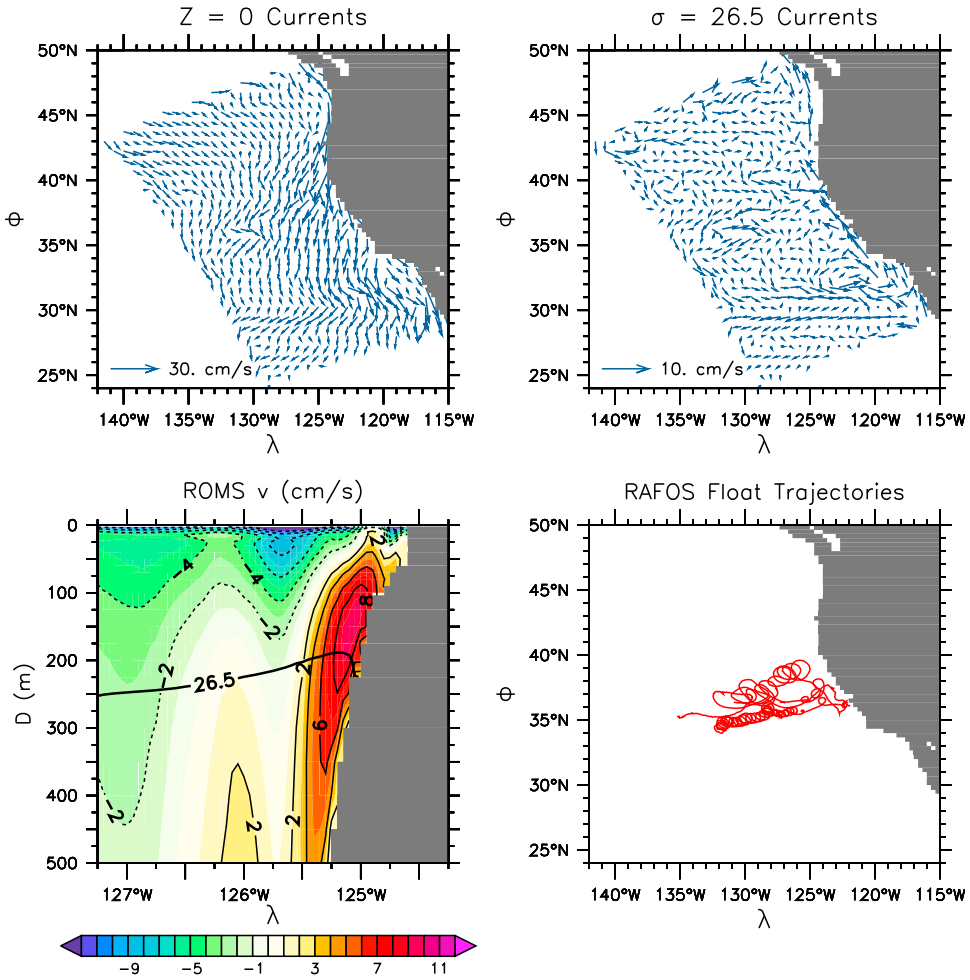

Figure 1. ROMS annual mean currents at the (top left) surface (z = 0 m) and (top right) subsurface (σ = 26.5 kg/m^3). (bottom left) Summer mean meridional velocity (v) along 42°N from ROMS and (bottom right) the trajectory of a few selected RAFOS float measurements [*Garfield et al.*, 1999]. Axis labels are longitude λ (°W), latitude ϕ (°N), depth D (m).

anticyclones with a subsurface core (~400 m) [*Simpson and Lynn*, 1990; *Huyer et al.*, 1998; *Garfield et al.*, 1999; *Shearman et al.*, 1999; *Brink et al.*, 2000; *Chereskin et al.*, 2000; *Cornuelle et al.*, 2000; *Jerónimo and Gómez-Valdés*, 2007]. Though the observed water properties in the eddies tend to confirm this idea, salinity anomaly of subsurface anticyclones are not always distinctively high, due to mixing within the undercurrent [*Reed and Halpern*, 1976]. In addition, they may not have any surface expression in temperature and salinity fields, but can be apparent in surface currents [*Brink et al.*, 2000]. Eddy effects are visible down to about 400 m depth for surface eddies and to about 1000 m depth for subsurface eddies [*Simpson and Lynn*, 1990; *Huyer et al.*, 1998; *Shearman et al.*, 1999; *Chereskin et al.*, 2000; *Jerónimo and Gómez-Valdés*, 2007]. Reported eddy radii are in the range of 40–60 km. Subsurface anticyclones are known to survive for significant time (on the order of months) and travel considerable distance offshore [*Lukas and Santiago-Mandujano*, 2001] with speeds about 1.0–1.7 km/day [*Huyer et al.*, 1998; *Garfield et al.*, 1999; *Collins et al.*, 2003]. Analysis of RAFOS floats have shown that maximum undercurrent velocity is seen during late summer [*Collins et al.*, 2003]. These eddies are strongly nonlinear [*Chereskin et al.*, 2000; *Cornuelle et al.*, 2000] and hence are very efficient in transporting the distinct undercurrent water to offshore. There are hardly any observations of cyclones with subsurface core and reports on surface eddies are very limited.

[5] Recently, eddy detection and tracking algorithms using altimetry data have shown to be extremely useful tool to study mesoscale eddies in both space and time [*Isern-Fontanet et al.*, 2003; *Chelton et al.*, 2007, 2011]. Global and regional application of such algorithms were successful in characterizing different aspects of mesoscale eddies (e.g., size, polarity, westward propagation, and lifetime). *Stegmann and Schwing* [2007] and *Chaigneau et al.* [2009] used such algorithms to study the CCS eddies and found there is no significant difference between eddy polarities in terms of size and propagation speed. It is also shown that the formation of long-lived eddies and eddy activity are greatest roughly between latitudes 32°–40°N, with a distinct minimum to the north of about 42°N. There are few key eddy generation sites along the coast; these sites include Punta Eugenia (~28°N), Point Conception (~34°N), and Cape Blanco (~43°N). Both studies report less seasonal variation in eddy birth, though the eddy strength is highest

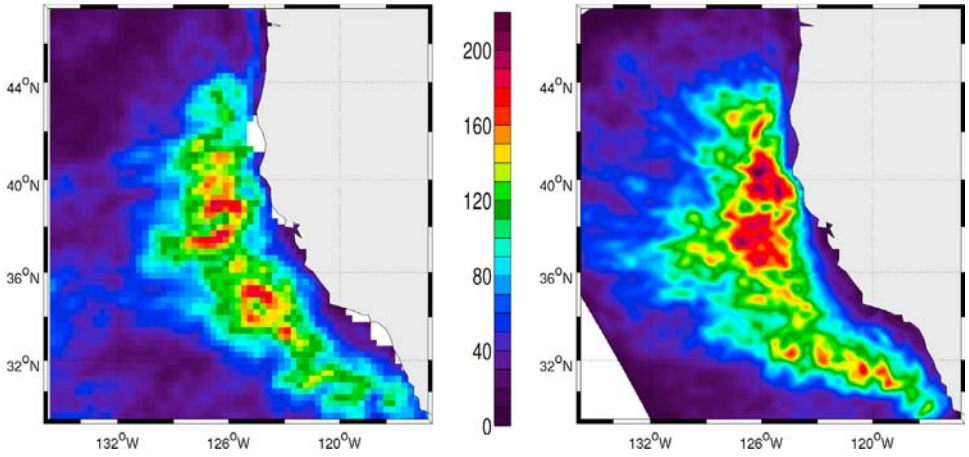

Figure 2. EKE (cm^2/s^2) computed from the altimetry (left) measurements (improved Developing Use of Altimetry for Climate Studies SSH product for the period 2001–2006 [*Pascual et al.*, 2006]) and (right) model. The model EKE is computed using low-pass filtered (6-day averaging and Gaussian spatial filter with 30 km half-width) geostrophic velocities [adapted from *Capet et al.*, 2008].

during summer. Eddies propagate westward, with cyclones (and anticyclones) showing a general tendency for poleward (and equatorward) deflection, as shown globally by *Chelton et al.* [2007, 2011] and for the CCS region by *Morrow et al.* [2004]. Eddy radii of approximately 60–80 km and propagation speeds around 2 km/day have been reported.

[6] Application of such eddy detection and tracking algorithms with realistic high-resolution numerical model outputs increase the possibilities in the study of mesoscale eddies many fold. In addition to a better spatial/temporal resolution, model outputs offer the opportunity to study both the surface and subsurface eddies as well as their three-dimensional structure. In this study we employ such a strategy to study the properties of eddies in the CCS. However, a model has its own limitations too and hence we also address a comparison between eddies tracked from the model with those from the altimetry data set. The rest of this article is organized as follows: details of the ocean model configuration, model evaluation, and the altimetry dataset are presented in section 2. The automated eddy detection and tracking method is presented in section 3. Eddy statistics computed using the sea surface height (SSH) anomaly field from the model and the altimetry are compared in section 4. Eddy properties like size, strength, lifetime, propagation characteristics, occurrence, polarity, birth and death, and vertical structure are presented in section 5. A summary of the results is provided in section 6.

2. Model and Data Sets

[7] The Regional Oceanic Modeling System (ROMS) [*Shchepetkin and McWilliams*, 2005; *Haidvogel et al.*, 2009] is configured to simulate a realistic quasi-equilibrium solution of the CCS [*Capet et al.*, 2008]. The present configuration can be considered as an evolution of the ROMS U.S. West Coast setup of *Marchesiello et al.* [2003]. The model domain covers the entire U.S. West Coast, from 30°N to 50°N, and it extends more than 1000 km offshore. It has a horizontal grid resolution of 5 km and 32 vertical σ levels. Atmospheric forcing is climatological: heat and freshwater fluxes are monthly mean fields from Comprehensive Ocean-Atmosphere Data Set [*da Silva et al.*, 1994] and monthly mean wind stress is computed from Quick Scatterometer (QuikSCAT) data. Open boundary information is taken from a monthly climatology computed from Simple Ocean Data Analysis (SODA) [*Carton and Giese*, 2008]. The open boundary conditions follow the machinery described by *Marchesiello et al.* [2001]. The model is integrated for 12 years, with the model fields archived as 2 day averages. The first 3 years are taken as spin-up and discarded from the analysis.

[8] The model realistically simulates the known features of the CCS. The CC at the surface and the California Undercurrent at subsurface are well represented in the model (Figure 1 and section 1), with realistic magnitudes and seasonal cycles. However, the mean model currents are weak in the northwestern part of the domain where the North Pacific Current extends to form the CC (Figure 1, top left). The coastal upwelling, its seasonal cycle, and features like the coastal jet in the model match well with the observations. However, the model thermocline is slightly diffused compared to the observations (not shown). The model has rich mesoscale activity with the formation of jets, filaments, and eddies as seen in satellite observations [*Kelly et al.*, 1998]. To validate the model mesoscale activity, surface eddy kinetic energy (EKE) from the model is compared with that computed from altimetry observations in Figure 2 (adapted from *Capet et al.* [2008]). A point-wise comparison between the model EKE and the altimetry derived EKE is meaningless due to the differences in spatial resolution and inherent sampling errors. It requires data for many decades for an accurate analysis of point-wise eddy variance [*Flierl and McWilliams*, 1977]. Moreover, model solutions should be processed in the same way as the altimetry data for a precise comparison. Given these limitations, there is general agreement between observed and modeled EKE in terms of magnitude and spatial patterns (nearshore minimum and offshore maximum). However, there are localized differences, like stronger EKE magnitude in the model between 30°–42°N, which could be attributed to the complex processes involved in EKE generation [*Capet et al.*, 2008]. The model also reproduces the seasonal offshore migration of maximum

surface EKE from spring through winter (not shown), as seen in observations [*Kelly et al.*, 1998]. The themohaline structure and circulation in the CCS are also well represented in the model [*Capet et al.*, 2008].

[9] The SSH anomaly dataset, called the merged Maps of Sea Level Anomalies (MSLA), from Archiving, Validation, and Interpretation of Satellite Oceanographic data (AVISO) on a 1/3° × 1/3° grid during 1992–2008 is used for this study. This "reference series" dataset uses only two missions at a given time and hence is stable and homogeneous throughout the analysis period. Data is used as provided without any special filtering to remove large scale variations (e.g., steric heating and cooling). Only the data within the model domain (Figure 1, top) is used for the present work.

3. Eddy Detection Methods

[10] Several different methods have been developed for detecting eddies from satellite altimetry and model simulations. In general they fall into two categories: physics-based methods and geometrical methods. Physics-based methods involve the calculation of dynamical fields and have an eddy definition based on closed contours of a threshold value. Different fields like the SSH anomaly [*Palacios and Bograd*, 2005; *Stegmann and Schwing*, 2007; *Henson and Thomas*, 2008; *Chaigneau et al.*, 2009; *Chelton et al.*, 2011], vorticity (ζ) [*McWilliams*, 1999], and velocity gradient tensor (Q) or Okubo-Weiss parameter (W) [*Isern-Fontanet et al.*, 2003, 2004; *Morrow et al.*, 2004; *Chelton et al.*, 2007; *Sangrà et al.*, 2009] have been used. Geometrical methods use the curvature or shape of the instantaneous flow field to detect eddies. Examples include the winding angle based approach with streamlines [*Sadarjoen et al.*, 1998] and the vector geometry based method [*Nencioli et al.*, 2010]. Methods based on wavelets [*Luo and Jameson*, 2002; *Doglioli et al.*, 2007; *Sangrà et al.*, 2009] and Lagrangian coherent structures [*Beron-Vera et al.*, 2008] were also used for eddy detection. Among these, the closed contour method with SSH or W (equivalently Q) remains the most popular owing to its simplicity and computational efficiency. We have used the closed contour method, based on both Q and SSH, with the details given in the following sections.

[11] There is no universally accepted best method for detecting an eddy from either water or flow properties. Even with carefully devised detection rules, the definition of an ideal eddy is somewhat elastic among different scientists, and subjective judgments about how to measure departures from the ideal and how large is acceptable lead to nonunique eddy detections. This situation is inherent in algorithmic pattern recognition algorithms and other forms of artificial intelligence. Our own methods, as others, have evolved from many tests pitting objective detection against our visual identification.

3.1. Q and SSH Methods

[12] The Q parameter represents the second invariant of the velocity gradient tensor. According to *Isern-Fontanet et al.* [2003], it can be expressed in the following form for planar flows

$$Q = -\left(\frac{\partial u}{\partial x}\right)^2 - \left(\frac{\partial v}{\partial x}\right)\left(\frac{\partial u}{\partial y}\right), \quad (1)$$

where u and v are eastward and northward velocities. The two terms on the right-hand side of equation (1) account for deformation and rotation, respectively; hence, for regions where rotation dominates deformation, $Q > 0$. In other words, eddy cores can be identified by connected regions (i.e., closed contours) of $Q > 0$. A similar expression can be derived from Okubo-Weiss parameter [*Okubo*, 1970; *Weiss*, 1991]:

$$W = S_n^2 + S_s^2 - \zeta^2, \quad (2)$$

where S_n, S_s, and ζ are the normal and shear components of the strain and the relative vorticity of the flow is expressed as

$$S_n = \frac{\partial u}{\partial x} - \frac{\partial v}{\partial y}, \quad S_s = \frac{\partial v}{\partial x} + \frac{\partial u}{\partial y}, \quad \zeta = \frac{\partial v}{\partial x} - \frac{\partial u}{\partial y}. \quad (3)$$

Assuming a horizontally nondivergent (planar) flow, i.e.,

$$\frac{\partial u}{\partial x} + \frac{\partial v}{\partial y} = 0. \quad (4)$$

W (equation (2)) can be reduced as follows [*Chelton et al.*, 2007]:

$$W = 4\left(\left(\frac{\partial u}{\partial x}\right)^2 + \left(\frac{\partial v}{\partial x}\right)\left(\frac{\partial u}{\partial y}\right)\right). \quad (5)$$

Regions where rotation dominates deformation will have $W < 0$. Except for a change of sign and a factor of 4, Q (equation (1)) corresponds to W (equation (5)). Eddy identification based on the Q and W fields will yield exactly the same results, provided corresponding contour values are used (i.e., $W = -4 \times Q$). Because Q has a short range of (positive) values, we opted to work with Q instead of W.

[13] The most common eddy identification procedure with either the Q/W- or SSH method is to treat the area within a closed contour as an eddy, and to test properties derived from the contour against specified constraints (e.g., size and amplitude). Different methods like circle/ellipse fitting or area and centroid calculation are used for defining eddy parameters based on the contour. Typically, the contour search is made for a specified threshold value, either defined as 0.2 times the standard deviation (with the standard deviation calculated at each time step for the entire domain) [*Isern-Fontanet et al.*, 2003; *Henson and Thomas*, 2008] or taken as a constant [*Chelton et al.*, 2007; *Stegmann and Schwing*, 2007]. This closed contour method approach can be criticized in several ways: (1) The field is too noisy (more so with W/Q derived from the SSH anomaly). (2) It detects too many bogus eddies (e.g., filaments). (3) It sometimes fails to detect well-formed eddies.

[14] The W or Q field can be very noisy especially if derived from the SSH [*Chelton et al.*, 2011] because the double differentiation amplifies noise in the original SSH anomaly data. However, with the model solution this is not a serious concern because velocity fields are not noisy. In addition, the W/Q method has the added advantage of tracking eddies at desired depth levels or isopycnal surfaces from the model solution. Spatial smoothing can arguably reduce the noise in the field used. In the present study multiple applications of a 2-D Hanning smoother is made on Q field derived from model, whereas SSH anomaly fields from both model and altimetry are used as is. To skip noneddy

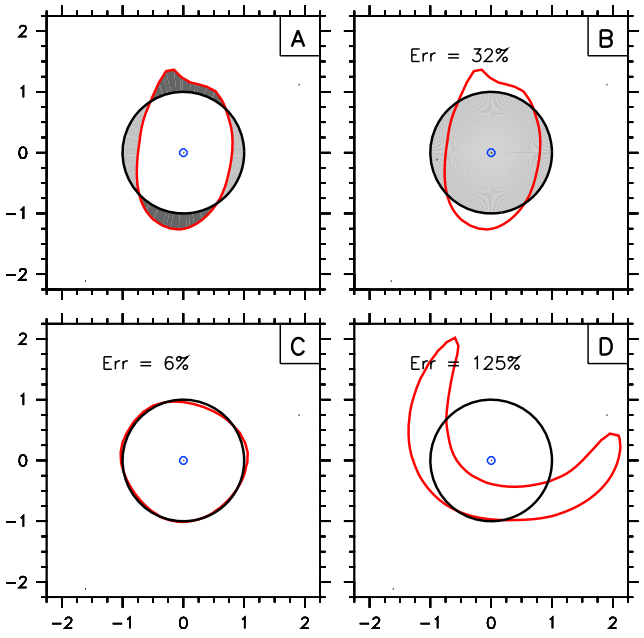

Figure 3. (a and b) Eddy shape error: A closed contour (red line) that deviates from the circular shape (black line, fitted circle) can have gap areas within the fitted circle (light shaded region in Figure 3a) and bulge areas outside (dark shaded region in Figure 3a). The eddy shape error is the sum of area deviations (sum of shaded regions in Figure 3a) expressed as a percentage of the area of the fitted circle (shaded region in Figure 3b). For a closed contour in a perfect circular shape, the shape error is 0%. (c and d) Extreme cases from ROMS: a near-circular eddy (Figure 3c) and a filament (Figure 3d). The horizontal scale is normalized (by radius) to get unit circles.

structures we introduced a shape test. Closed contours can have gap areas within the fitted circle (Figure 3a, light shading) and bulge areas outside (Figure 3a, dark shading). The shape error, defined as the ratio between the sum of the total area of deviations from the circle to the area of the circle (Figure 3b, light shading), is calculated for each closed contour. For a contour in perfect circular shape, this parameter will be zero. Based on case studies we chose only those closed contours with a shape error in the range 0–35% in the Q method and 0–50% in the SSH method to define eddies (Figure 3). Use of a single "threshold" value for the closed contour can sometimes fail even to detect even well-formed eddies. Instead, we use a realistic range of values for both the SSH anomaly and the Q fields to identify eddies as employed by *Chelton et al.* [2011].

[15] In the Q method the closed contour search is made from 5×10^{-11} s^2 onwards with fine spacing near the lower end. With the SSH method the search is made in a reverse order for cyclones and anticyclones, to handle situations where the eddy is embedded in large scale background SSH variations [*Chelton et al.*, 2011]. Cyclones are searched for from 50 cm to −50 cm with a contour interval of −1 cm. Anticyclones are searched for in opposite direction, starting at −50 cm and going to 50 cm with an interval of 1 cm. The outermost contour for each eddy that satisfies all the given criterion is chosen to define the outer edge of the eddy. For both methods, the center of the eddy is defined as the centroid of the closed contour of the respective parameter (Q or SSH). Radius for the SSH method is defined as the radius of a circle with the same area as that of the closed contour (Figure 4). The Q (or W) parameter defines the "vortex core" region; therefore, the estimation of the eddy radius based on closed contours of Q or W, tends to be smaller than an estimate based on dynamic height [*Isern-Fontanet et al.*, 2003; *Henson and Thomas*, 2008]. We define it as the minimum distance between the eddy center and the closest

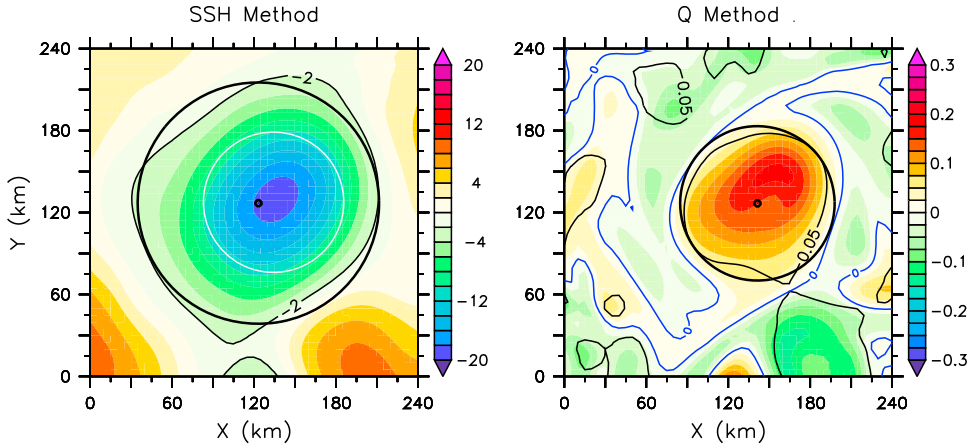

Figure 4. Eddy definition using the (left) SSH and (right) Q methods for a cyclonic eddy at surface. Color shading shows the SSH anomaly (cm; Figure 4, left) and ζ/f (Figure 4, right) with color bars. The thin black line shows the SSH anomaly and Q contours used for defining eddy shape and eddy center. The fitted circle is shown in thick black line and the eddy center in small open circles. The white contour line (Figure 4, left) shows the circle corresponding to eddy radius estimated by the maximum geostrophic speed-based method as by *Chelton et al.* [2011]. The blue contour line (Figure 4, right) shows the zero ζ/f line, where the radius is defined in the Q method. This example illustrates that the radius in the Q method (56 km) is usually less than that for the SSH method (88 km) and larger than the geostrophic speed-based method (51 km); these relations are explained in Appendix A.

zero contour of ζ/f. However, the eddy radius estimated with the Q method is usually less than that using the SSH method (Figure 4, in this example by about 64%), and the reason for this is explained in Appendix A. For comparison we have also made a geostrophic speed-based estimate of the eddy radius following *Chelton et al.* [2011]. In this method, eddy radius is defined as the radius of the circle that has the same area as that of the SSH anomaly contour (within the first identified outermost SSH contour) around which the average geostrophic speed is maximum (the corresponding circle is shown by the white contour line in Figure 4 (left)). For the example shown in Figure 4, the geostrophic speed-based radius estimate is somewhat smaller than that from the Q method. We choose to use a size estimator based on the field being analyzed, recognizing that this requires translation among the sizes determined by different methods in a way that depends on eddy shape (Appendix A).

[16] Eddy strength (amplitude) for the SSH method is defined as the difference between the extremum value for the SSH anomaly within the eddy and the identifying contour value. The eddy strength for the Q method is defined as the maximum of $|\zeta/f|$ within the eddy. Eddy polarity in the Q method is defined by the sign of ζ/f at the center of the eddy (negative for anticyclones and positive for cyclones). With the SSH method, polarity is determined by whether the SSH anomaly is decreasing (cyclones) or increasing (anticyclones) toward the eddy center.

[17] After the shape error, radius, and amplitude are computed for a closed contour, the following tests are made: (1) The shape error of the closed contours should be below 35% in the Q method and below 50% in the SSH method. (2) All data points inside the closed contour should be nonland. (3) ζ/f on all grid points inside the closed contour of Q should be of the same sign in the Q method, and the SSH anomaly magnitude should monotonically increase toward the center in the SSH method. (4) The radius should be within 15–150 km for the Q method and 45–150 km for the SSH method (the resolution capability of the AVISO "Reference" dataset is ~45 km at equator [*Chelton et al.*, 2011]). (5) The eddy amplitude should be ≥1 cm for the for the SSH method and ≥0.02 for the Q method.

[18] Those closed contours that pass all of the tests above are accepted as eddies.

3.2. Eddy Tracking

[19] Eddies are tracked using an automated procedure, by comparing eddy centers and properties at consecutive time levels (t_n & t_{n+1}) for the entire time series in both the Q and SSH methods. A given eddy at time level t_n is tracked at time level t_{n+1} by finding the closest eddy center at t_{n+1}. To avoid switching between tracks, the distance between the eddy centers at t_n and t_{n+1} are required to be less than the sum of eddy radii during two successive time levels. The change in eddy amplitude and area from t_n to t_{n+1} should be within 0.25–2.5 of their value at t_n [*Chelton et al.*, 2011]. These criteria assure that the characteristics of a tracked eddy evolve slowly over time. No condition is imposed on the direction of the search (i.e., the direction of the eddy propagation). Eddy splitting or merging situations are not handled separately. The nearest eddies with the minimum change in amplitude and area are always assigned to a common track.

3.3. Distinct Subsurface Eddies

[20] With model results eddy tracking can be performed with surface and subsurface fields. In practice we chose to do it for surface ($z = 0$ m, units will be skipped hereafter) and also on the 26.5 isopycnal ($\sigma = 26.5$ kg/m^3, units will be skipped hereafter) that corresponds to the core of the California Undercurrent (Figure 1, bottom left). Because eddies have a deep vertical structure, surface-generated eddies can have signatures at deeper depths (>400 m), and conversely subsurface-generated eddies can have signatures at the surface. To avoid double counting of eddies, we have tested two different methods to distinguish between surface- and subsurface-generated eddies. In the first method, the eddy core depth (the depth at which $|\zeta/f|$ is maximum, estimated from the vertical profile at the eddy center) is required to be shallower than 80 m during at least 70% of the eddy lifetime (L) for a surface-generated eddy and deeper than that for a subsurface-generated eddy. This method retains only very few subsurface-generated cyclones (9 with L ≥ 90 days and birth within 250 km from the coast, on the $\sigma = 26.5$ level), insufficient for any analysis. In fact, no cyclones with a distinct subsurface core are observed in the eddy dataset, and those tracked on the $\sigma = 26.5$ level are subsurface manifestations of cyclones generated at the surface. However, it is instructive to analyze cyclones tracked at subsurface level to know the eddy properties at the subsurface level.

[21] In the second method, we keep all the tracks at $z = 0$ as surface-generated eddies, but remove those tracks at $\sigma = 26.5$, which are similar to that at $z = 0$. This is motivated by the observation that the surface expression of subsurface-generated eddies are not always strong and may not be continuous in time. This is particularly true for longer lived subsurface-generated eddies. In addition, the subsurface expression of surface eddies may extend deeper than the $\sigma = 26.5$ level. Eddy tracks at $z = 0$ and $\sigma = 26.5$ are defined as common tracks, if (1) they exist simultaneously for a "common time period", which is at least 50% of the longest L among them, and (2) for at least 70% of the common time period, the distance between the eddy centers (at each snapshot; snapshot is the time slice of the data at its archival frequency, 2-day average for model fields and 7-day average for altimetry SSH) is less than the minimum radius between the two levels.

[22] The definition of the common tracks above is not very sensitive to the cutoff percentages used here. The common time period criterion above will assure that only those eddies that appear at both $z = 0$ and $\sigma = 26.5$ levels will consistently be labeled as common eddies. For the $\sigma = 26.5$ case, these common tracks are removed to have the distinct tracks, which are considered for the analysis presented in section 5. Compared to the first method, this method retains more cyclones at subsurface (56 with L ≥ 90 days and birth within 250 km from the coast, on the $\sigma = 26.5$ level). However, the subsurface cyclones identified using this method should be treated as the subsurface expression of surface-generated cyclones.

4. Model to Altimetry Comparison of the Eddy Field

[23] For a model altimetry comparison, we present a few selected results from the SSH method. We use the SSH

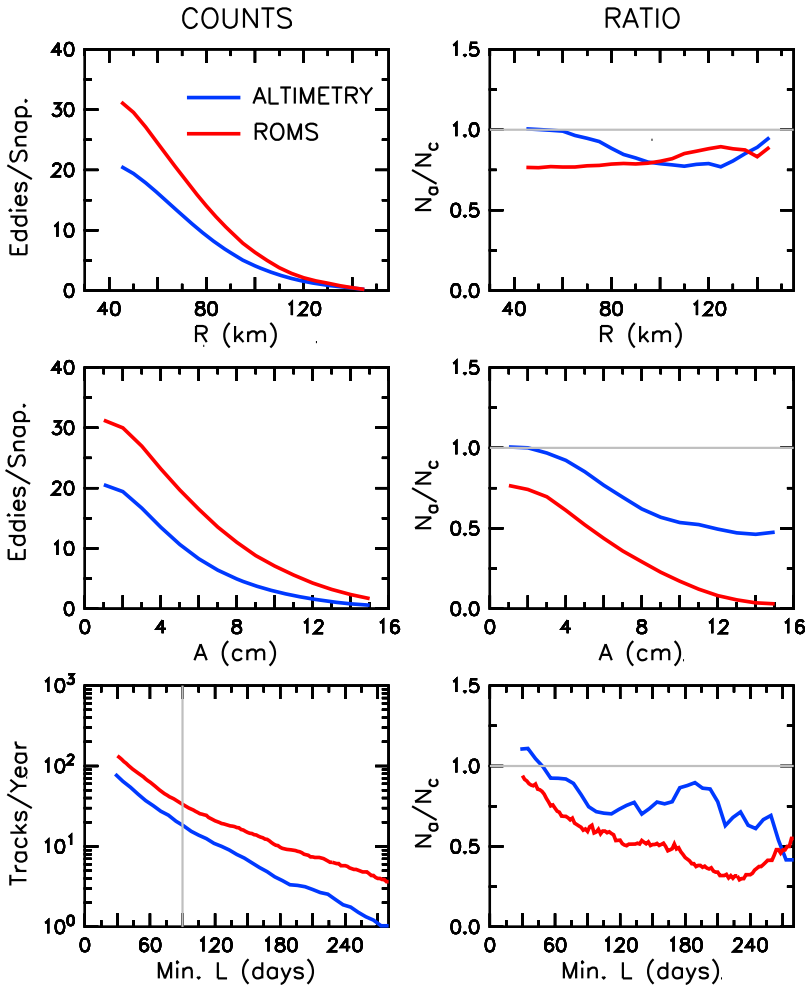

Figure 5. (top and middle) Cumulative eddy count per snapshot (snapshot refers to 2-day average data for model (ROMS) and weekly data for altimetry) and (bottom) eddy track count per year binned with respect to radius (R, km; Figure 5, top), SSH, amplitude (A, cm; Figure 5, middle), and minimum lifetime (L, days; Figure 5, bottom). (left) Total counts $N = N_a + N_c$ (N_a is number of anticyclones and N_c is number of cyclones), and (right) polarity ratios N_a/N_c. Binning is cumulative suchthat the counts also include eddies with higher values of the property. Only those eddies with $L \geq 28$ days are included.

method for this purpose since there is no need for differentiation of the altimetric SSH anomaly field. For a fair comparison, identical parameters (like minimum radius) are used for both altimetry and the model. Only three main eddy properties (size, strength, and abundance) are considered, for eddies with $L \geq 28$ days. Eddy strength (amplitude) for the SSH method is defined as the difference between the maximum (minimum) value of the SSH anomaly within the eddy and the contour value for anticyclones (cyclones). Values from each snapshot are used for radius and amplitude, without averaging over the track/life period.

[24] Eddy radii (R) in both the model and altimetry vary within 45–150 km (the range set in the eddy identification routine), and the number of eddies decreases with increasing R (Figure 5, top left). The decline in number of eddies (per snapshot) is more pronounced in the R range of 45–100 km, in the both model and altimetry. On average, there is only one eddy per snapshot with $R \geq 130$ km. Compared to altimetry, the model has more eddies in all size ranges. Both the model and altimetry shows cyclonic dominance (Figure 5, top right), especially for higher R. However, the altimetry data do not show any polarity preference in the R range of 45–70 km, whereas the model exhibits cyclonic preference in the whole range of R. Both the higher number of eddies in the model and cyclonic dominance at smaller R can be explained by the smaller scales resolved by the model and a less noisy model SSH field compared to altimetry.

[25] The eddy SSH anomaly amplitude (A) (section 3.1) varies in the range 1–15 cm (Figure 5, middle left) (1 cm is the minimum A required by the eddy identification routine), with few instances where it reaches values higher than 25 cm. The number of eddies (per snapshot) decreases with increasing A in both the model and altimetry, with a sharp decline between A in the range 1–9 cm. On average, there is about 1 eddy with $A \geq 13$ cm in the altimetry, whereas there are about 3 eddies in the model in a single snapshot. There are more eddies in the model at all values of A, compared to the altimetry. Eddy polarity ratio shows cyclonic dominance (Figure 5, middle right), except for a neutral situation in the altimetry case for A in the range 1–3 cm. Cyclonic domi-

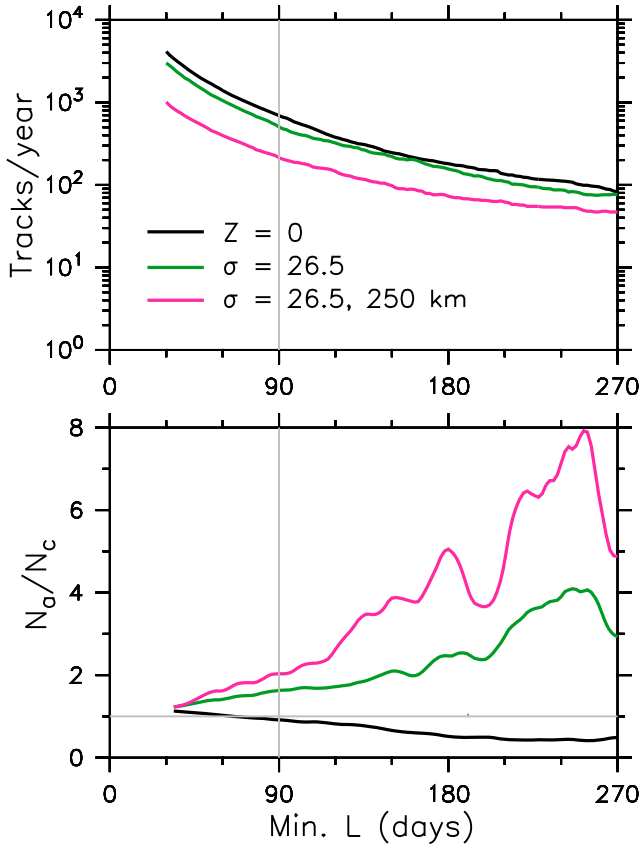

Figure 6. Cumulative distribution (i.e., number of eddies with L ≥ to any given L on the X axis) of (top) an eddy track count and (bottom) a polarity ratio for z = 0 m (black), σ = 26.5 kg/m^3 (green), and the subset of σ = 26.5 eddies generated within 250 km from the coast (violet) from ROMS. The polarity ratio is smoothed by a 4-point boxcar filter.

nance increases with increasing A, which could result from weakening of the anticyclones by centrifugal instability [*Sipp et al.*, 1999]. The polarity ratio also shows that the model has stronger cyclonic dominance throughout the range of A, a result of resolving finer scales in the model.

[26] The number of eddy tracks also has similar patterns between the model and altimetry (Figure 5, bottom left). The number of eddy tracks (per year) decreases with increasing minimum L. In general, for a given minimum L, the model has about twice the number of eddy tracks in the altimetry (at minimum L = 90 days there are 33 tracks/year in the model and at minimum L = 91 days, there are 18 tracks/year in the altimetry). Both the model and altimetry shows cyclonic dominance with the number of tracks (Figure 5, bottom right), except for the anticyclonic dominance at lower minimum L (≤49 days) in the altimetry. The model tendency for stronger cyclonic dominance is also visible in the polarity ratio.

[27] We find there is general agreement in eddy property distribution between the model and altimetry in terms of eddies tracked using the SSH method. Distributions of eddy radii, amplitude, and lifetime show that more of the eddies have a smaller size, weaker amplitude and shorter lifetime. The eddy polarity ratio shows that, in the CCS, there are more cyclones at the surface. There are differences between the model and altimetry in terms of the number of eddies (higher in the model) and eddy polarity (strong cyclonic dominance in the model). In addition, altimetry data do not show any polarity preferences with smaller size eddies and with weaker eddies. These differences mainly arise from finer scales resolved by the model and a less noisy model SSH field.

5. Eddy Properties

[28] In this section we analyze the properties of eddies at the surface and subsurface, identified with the Q method from the model fields. A detailed description of eddy properties (defined in section 3) is provided in this section. Eddies with L < 30 days are completely discarded from the analyzes, and suitable higher cutoff is applied wherever required (L ≥ 90 days for long-lived and L ≥ 180 days for very long-lived eddies). Also, the eddy identification is done with a minimum radius cutoff at 15 km and a maximum cutoff at 150 km. Eddy strength (amplitude) for the Q method is defined as the maximum of $|\zeta/f|$ within the eddy; the eddy boundary is set by the zero contour of ζ/f. Eddy properties for both surface and subsurface levels and for both polarities are presented side by side.

5.1. Abundance, Polarity, Size, and Strength

[29] Cumulative distributions with size L (i.e., number of eddies with minimum size ≥L) and the anticyclone/cyclone ratio for eddies tracked at both surface and subsurface levels are in Figure 6. At z = 0 (black line), there are 4133, 691, and 181 eddies with L ≥ 30, 90, and 180 days, respectively. Only 36 eddies lived longer than 360 days. The number of eddies decreases sharply with increasing L, especially for L < 90 days. The eddy count distribution for σ = 26.5 (green line) is similar to that at z = 0, but with a fewer number of eddies at all L. There are 3006, 503, and 156 eddies with L ≥ 30, 90, and 180 days. Only 47 eddies have lifetime above 360 days. The asymmetry in polarity at surface is clearly seen in the ratio of the number of anticyclones to cyclones (Figure 6, bottom). There is a strong cyclonic dominance at surface for long-lived eddies. The anticyclone/cyclone ratio is 0.91 and 0.52 at minimum L of 90 and 180 days. After L = 180 days, the ratio remains around 0.4. At the subsurface, considering the whole domain, there is anticyclonic dominance at all L, with an anticyclone/cyclone ratio of 1.62 and 2.48 at minimum L of 90 and 180 days.

[30] To isolate the undercurrent-generated eddies, the cumulative probability density functions (pdf) of L, and the polarity ratio for σ = 26.5 eddies generated within 250 km of the coastline is also shown in Figure 6 (violet line). There are 1011, 213, and 73 eddies formed within 250 km of the coastline with a minimum L of 30, 90, and 180 days. Among long-lived eddies, 31 have L above 360 days. About 33%, 42%, 47%, and 66% of the σ = 26.5 anticyclones are generated within 250 km for a minimum L of 30, 90, 180, and 360 days. This clearly shows that a majority of the long-lived anticyclones in the CCS are formed near the coast. No such clear pattern exists for the subsurface cyclones. The eddy polarity ratio clearly shows the strong dominance of anticyclones at all L, with values of about 2 and 5 at minimum L of 90 and 180 days. To summarize, the subsurface eddies developed near the coast by the undercurrent are

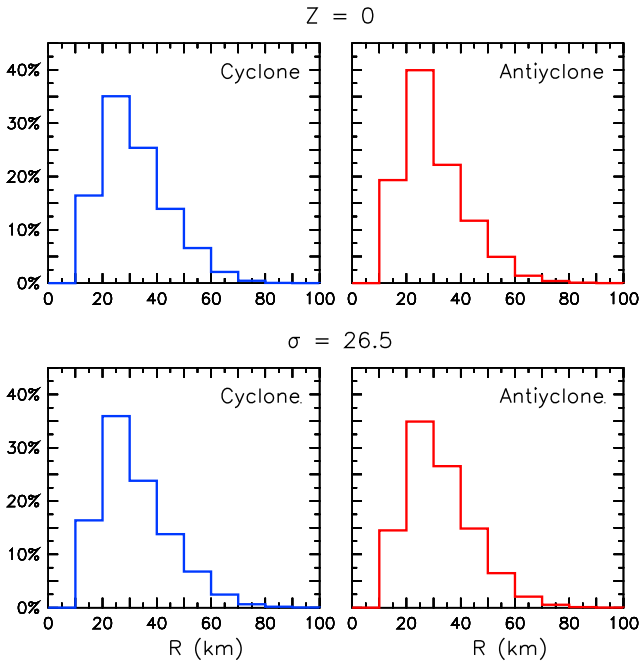

Figure 7. Pdf of eddy radius (R) from ROMS using the Q method.

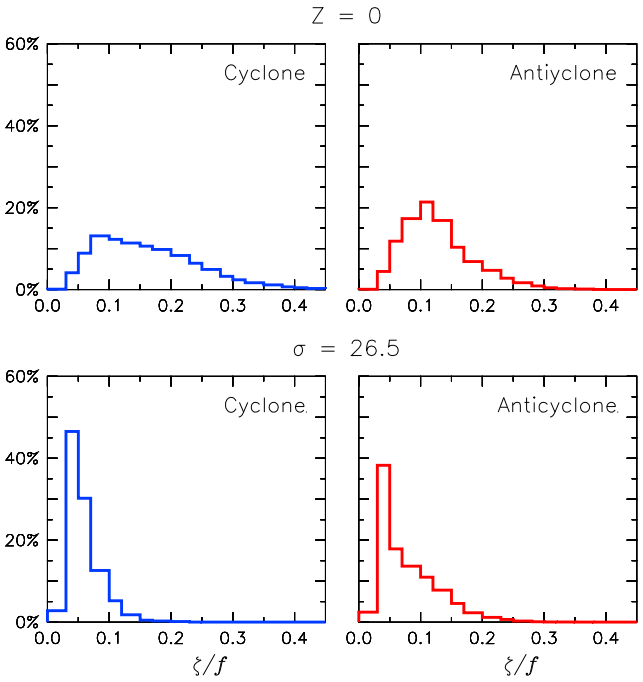

Figure 9. Pdf of eddy strength (maximum of $|\zeta/f|$) from ROMS, using the Q method.

predominantly anticyclonic, which is in very good agreement with the RAFOS float observations by *Garfield et al.* [1999].

[31] The pdf of eddy radius is in Figure 7. Eddies have a radius in the range 15–70 km, with the peak at 20–30 km. There is no striking difference between radius distribution among the polarities and between the surface and subsurface levels. The surface anticyclones have slightly smaller percentage of eddies with radii above 40 km (18%), compared cyclones at surface and both polarities at subsurface (23–24%). Additional diagnostics (not shown) demonstrate that there is no robust relation between eddy size and the formation season. Eddy radii do not show any steady change with latitude. However, eddies with radius above 35 km are very rarely seen to the north of 38°–40°N, especially in case of cyclones. While the model shows many long-lived eddies to the north of 40°N near the coast (Figure 10), our own altimetry analysis (not shown) and that in previous studies [*Stegmann and Schwing*, 2007; *Chaigneau et al.*, 2009] do not have many eddies (with L ≥ 35 days) in this part of the CCS. Present analysis with the model shows that this may be partly due to the resolution limitations of the altimetry dataset. Eddy radii are smaller near the coast compared to those offshore (Figure 8). Average radii are around 23 km near the coast and sharply increase to values around 33 km at 350 km offshore. This increase in eddy size can be attributed to the eddy formation from processes with smaller spatial scales near the coast and the inverse cascade while eddies move westward to the offshore region. Beyond 350 km offshore, mean eddy radii remain either almost steady ($z = 0$ cyclones, and $\sigma = 26.5$ anticyclones) or undergo gradual change ($z = 0$ anticyclones and $\sigma = 26.5$ cyclones).

[32] The pdf of eddy strength $|\zeta/f|$ is shown in Figure 9. Eddies at the surface are stronger, with values in the range

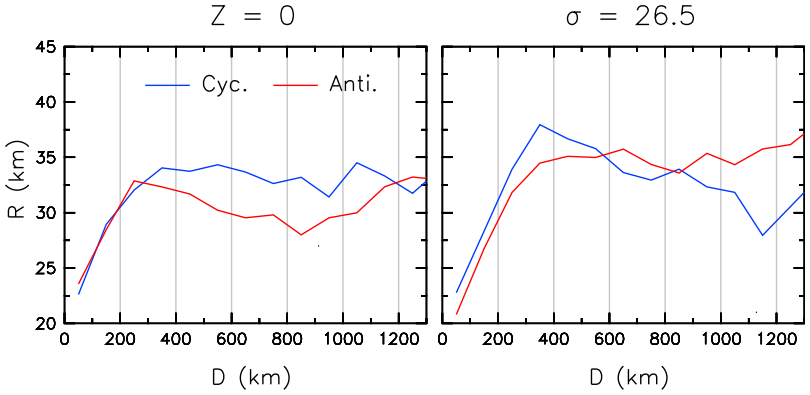

Figure 8. Alongshore-averaged eddy radius (R) as a function of the distance from the coast (D), using the Q method from ROMS.

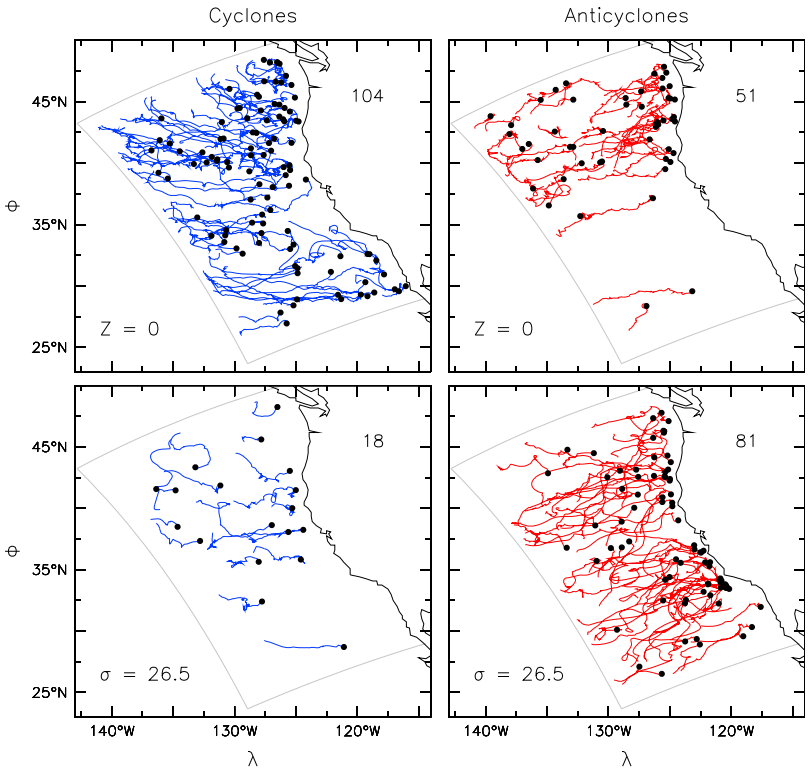

Figure 10. Tracks of long-lived (lifetime (L) ≥ 180 days) eddies with $\Delta\lambda \geq 1°$ from ROMS. Track counts are in top right of each panel. The black dots show the eddy birth location. Axis labels are longitude λ (°W) and latitude ϕ (°N).

0.0–0.5 and with a flat distribution. While about 30% of the surface cyclones have a ζ/f amplitude above 0.2, only 11% of surface anticyclones fall in this category. One possible cause for this could be centrifugal instability, which can weaken anticyclonic eddies [*Sipp et al.*, 1999]. Subsurface eddies have a ζ/f amplitude in the range 0.0–0.25, with cyclones peaking around 0.03–0.07 and anticyclones peaking around 0.03–0.05. A higher percentage of anticyclones (~27%) have a ζ/f amplitude above 0.1 than do cyclones (~8%). Thus, comparing the eddy polarities, more of the cyclones are stronger at surface, and more of the anticyclones are stronger at subsurface. The cyclones are weaker at subsurface level, because their core is at the surface (section 5.9); whereas, subsurface anticyclones have their core at subsurface, resulting in a higher ζ/f value.

5.2. Eddy Tracks

[33] Tracks of very long-lived eddies (L ≥ 180 days, with minimum longitudinal displacement of 1°; section 5.3) are shown in Figure 10. Many of the eddy properties (like westward propagation, meridional deflection, spatial patterns in birth locations) are visible from these eddy tracks, which will be discussed in following sections. Comparing eddy tracks at the surface and subsurface, there is a great deal of difference between cyclones and anticyclones. Most of the long-lived cyclone tracks are at the surface level, but those for the anticyclones are at the subsurface level (please note that only distinct eddies (section 3.3) are included for subsurface case). A majority of the long-lived eddies cross almost the entire model domain. The high nonlinearity (section 5.4) of these eddies imply that they can trap water and materials inside and efficiently transport them considerable distance offshore. Only a few very long-lived anticyclones are present to the south of 38°N at the surface, and this needs further investigation. There are no high density eddy track zones in the CCS, as observed in the North Atlantic [*Sangrà et al.*, 2009]. The region off San Francisco is lightly populated with eddy tracks, especially in the case of subsurface anticyclones. Also there are few subsurface anticyclonic tracks across the Southern California Bight, compared to the surface cyclones.

5.3. Westward Propagation

[34] Eddies show a strong tendency for westward propagation, with cyclones exhibiting a poleward deflection and anticyclones exhibiting a equatorward deflection from their due west path, as noted in previous studies [*Morrow et al.*, 2004; *Chelton et al.*, 2007, 2011]. This meridional deflection arises mainly from the beta effect and self-advection [*McWilliams and Flierl*, 1979; *Cushman-Roisin*, 1994]. To study the westward propagation characteristics, we consider only the surface cyclones and subsurface anticyclones (their counterparts would have similar propagation characteristics). For the sake of the robustness of the analyzes only very long-lived eddies (L ≥ 180 days) with a minimum longitudinal displacement of 1° are considered. The second criteria filters out standing eddies and those eddies that come back to their birth longitude (they do not have a meaningful propagation direction). About 13% of cyclones at $z = 0$ and anticyclones at $\sigma = 26.5$ (with L ≥ 180 days) belong to this category. The displacement angle (θ) is the angle of the line fitted to the eddy track, relative to west.

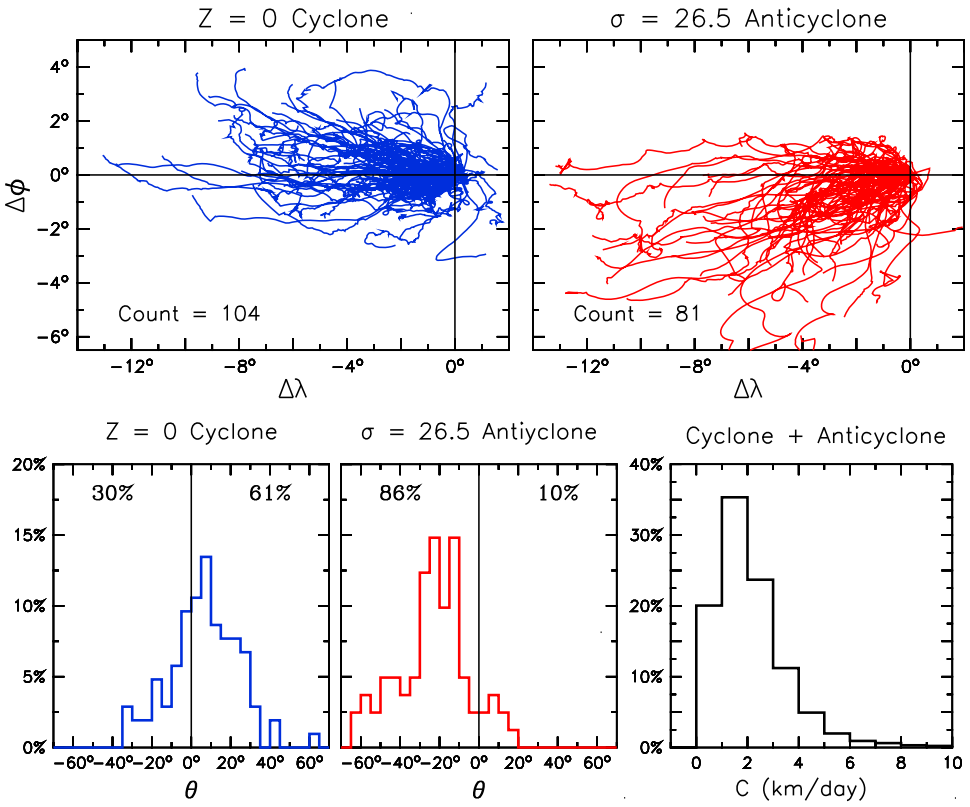

Figure 11. Propagation characteristics of $z = 0$ cyclones (blue) and $\sigma = 26.5$ anticyclones (red) with lifetime L ≥ 180 days and $\Delta\lambda \geq 1°$: (top) trajectories relative to birth location, and (bottom left) the pdf of displacement angle θ relative to the west and (bottom right) the pdf of bulk propagation speed C (km/day) from ROMS. The pdfs shown in the lower panels do not include eddies with eastward propagation or a near zonal path (9% of $Z = 0$ cyclones and 4% of $\sigma = 26.5$ anticyclones belong to this category). $\Delta\lambda$ and $\Delta\phi$ are longitudinal and latitudinal displacements (°).

[35] Eddy tracks referenced to a common starting point are given in Figure 11 (top). Model eddies show a strong tendency for meridional deflection. About 61% of the cyclones show a poleward deflection during their westward propagation, while about 30% deflect equatorward with the rest moving either eastward or taking a near zonal path (Figure 11, bottom left). Anticyclones show a stronger meridional deflection tendency with 86% deflecting equatorward while only 10% deflect poleward. There is a similar distinction between more equatorward anticylone tracks and more poleward cyclone tracks in the altimeter data in this region; however, both populations are more equatorward than in the model [*Chelton et al.*, 2011]. This difference between the altimetry and model likely results from a weaker mean current in the model to the north of about 38°N (section 2 and Figure 1 top left). In this region, where the North Pacific Current extends to form the CC, annual mean zonal velocity from the drifter climatology [*Lumpkin and Garraffo*, 2005] is about 4.6 cm/s, while it is only about 3 cm/s in the model. The propagation speed (combined for $z = 0$ cyclones and $\sigma = 26.5$ anticyclones because they show a similar pdf) varies in the range of 0–10 km/day, with a peak of about 1–2 km/day, which is in agreement with previous studies [*Stegmann and Schwing*, 2007; *Chelton et al.*, 2011] (Figure 11, bottom right). About 36% of the eddies are within the 1–2 km/day range, and about 20% have speeds exceeding 3 km/day. Thus, the westward propagation speed of eddies is comparable to the speed of nondispersive baroclinic Rossby waves (about 1 km/day at 40°N [see *Chelton et al.*, 2007]).

5.4. Nonlinearity

[36] The eddy nonlinearity parameter (η) is defined as the ratio between swirl velocity (U) and propagation speed (c) [*Chelton et al.*, 2007, 2011]. $\eta > 1$ implies nonlinear eddies: the speed of rotation exceeds the speed of propagation, eddies can effectively "trap" water inside and transport water properties along their tracks [*Samelson and Wiggins*, 2006]. A pdf of η for eddies with L ≥ 90 days is shown in Figure 12. At the surface, about 99% of eddies are associated with significant nonlinearities. Global eddy analysis by *Chelton et al.* [2011] also shows a high nonlinearity for eddies in the CCS. A large percentage of the surface eddies show high values of η, for 84% of cyclones and 75% of anticyclones that have $\eta \geq 5$. Thus, more of the cyclones at the surface show a high degree of nonlinearity. Among subsurface eddies, 97.5% cyclones and 99% anticyclones are nonlinear, with 55% of the cyclones and 56% of the anticyclones showing a high nonlinearity ($\eta \geq 5$). This demonstrates that both the surface and subsurface eddies in

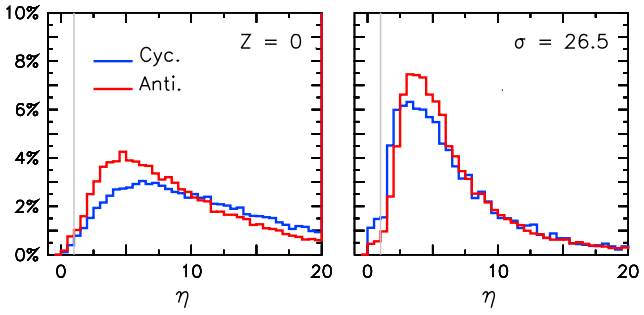

Figure 12. Pdf of the nonlinearity parameter (η, ratio between swirl velocity and propagation speed) for eddies with lifetime (L) ≥ 90 days from ROMS. The last bin also includes all values higher than the upper limit of that bin.

the CCS are capable of trapping water inside them and of transporting it offshore, and has implications on the offshore fluxes and the coastal ecosystem.

5.5. Distortion

[37] In general eddies defined by closed contour of properties are never in a perfect circular shape. This is the motivation for computing "shape error" (the ratio between the sum of the area deviations of the closed contour from the fitted circle to the area of the fitted circle, see section 3.1 and Figure 3) to decide to what extent eddies resemble to the fitted circle. Only eddies with shape error ≤35% are considered in the present analysis. The shape error is a good measure of eddy distortion; we have examined its pdf and spatial patterns. While there is no meaningful pattern with the pdf of the shape error (not shown), the percentage of eddies with less distortion (shape error ≤16) increases with increasing L. In other words, longer-lived eddies tend to be less distorted from a circular shape. Cyclones at the surface (with L ≥ 90 days) tend to be less distorted from the circular shape (47.4%) than those at subsurface (32.5%). While it is the opposite for anticyclones (39.5% for $z = 0$ and 51.9% for $\sigma = 26.5$ eddies): the difference is not as large as for cyclones. The shape error does not display any interesting spatial patterns.

5.6. Seasonal Cycle

[38] The seasonal cycle of surface as well as subsurface EKE peaks over the upwelling region of U.S. West Coast during summer and fall, with the minimum during spring [*Kelly et al.*, 1998; *Marchesiello et al.*, 2003]. However, the generation of eddies with L ≥ 30 days does not show any well defined seasonal cycle within the considered domain, as seen in previous studies [*Chaigneau et al.*, 2009]. Yet, very long-lived (L ≥ 180 days) anticyclones show a distinct peak during the winter (37%) and a minimum during the summer (10%). In contrast, the long-lived (L ≥ 90 days) σ = 26.5 eddies formed near the coast (within 250 km) show a well defined seasonal cycle (Figure 13). Anticyclone birth shows a peak during summer (37%) and a minimum during spring (13.5%). About 68% of the anticyclones are developed during the summer to fall seasons, and this is in general agreement with the seasons when the undercurrent is strongest. However, cyclones do not show much variation between seasons. The season with maximum anticyclone generation at the undercurrent level coincides with the season where the vertical shear in the undercurrent is strongest (not shown). This suggests that the baroclinic instability is an important mechanism for the generation of undercurrent eddies [*Marchesiello et al.*, 2003; *Capet et al.*, 2008].

[39] The eddy birth events (except for the subsurface undercurrent-generated anticyclones) do not have a close association with the seasonal cycle of mesoscale activity indices like EKE. However, measures of eddy strength (ζ/f, SSH anomaly, or EKE) show a summer peak near the coast and offshore propagation and spreading during the following seasons (Figure 14). Both for surface and subsurface eddies, ζ/f is highest during summer and fall, especially within 200 km from the coast. During fall, ζ/f for the surface eddies increases within the 100–500 km region offshore. During winter ζ/f drops near the coast, but it increases in the region offshore from about 200 km. Within the first 600 km offshore, ζ/f shows a decrease during spring, compared to the values during winter. This seasonal pattern and offshore migration of ζ/f for the surface eddies agrees well with the altimetry EKE analysis by *Kelly et al.* [1998]. For the subsurface eddies, the seasonal change near the coast is similar to that for the surface eddies. The offshore propagation is clearly visible for the subsurface anticyclones, but it is weaker for the subsurface cyclones, making it less apparent in the total field shown in Figure 14 (right).

5.7. Location and Polarity

[40] To identify regions of high eddy activity and corresponding polarities, we prepared spatial maps of eddy occurrence and polarity (Figure 15). Eddy occurrence (or frequency) is defined as the percentage of the total time where at least an eddy (of any polarity, with L ≥ 30 days) is present in a 1° × 1° box. Here, eddy polarity is defined as the difference between the number of anticyclones and cyclones binned as above, normalized by the total number of eddies observed in the corresponding binning box. Positive values for eddy polarity indicate the persistence of anticyclones, and negative values indicate the persistence of cyclones.

[41] At the surface and subsurface, eddy occurrence is relatively high (>25%) close to the coast over the entire domain, except a relative minimum off Monterey Bay at the surface. At $z = 0$, the offshore region to the north of 38°N also shows relatively high eddy occurrence (Figure 15). The

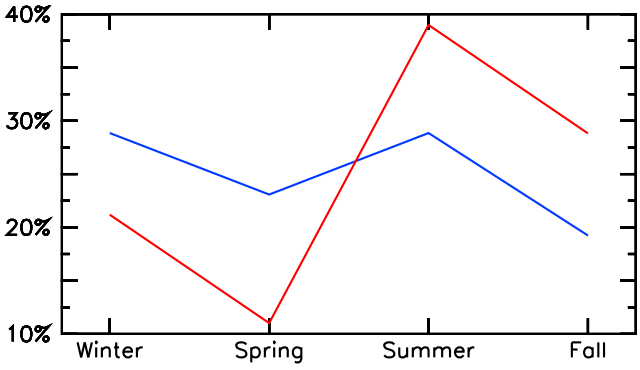

Figure 13. Seasonal percentages of cyclones (blue) and anticyclones (red) births at σ = 26.5 within 250 km from the coast and with lifetime (L) ≥ 90 days from ROMS. There are 56 cyclones and 111 anticyclones that meet these criteria.

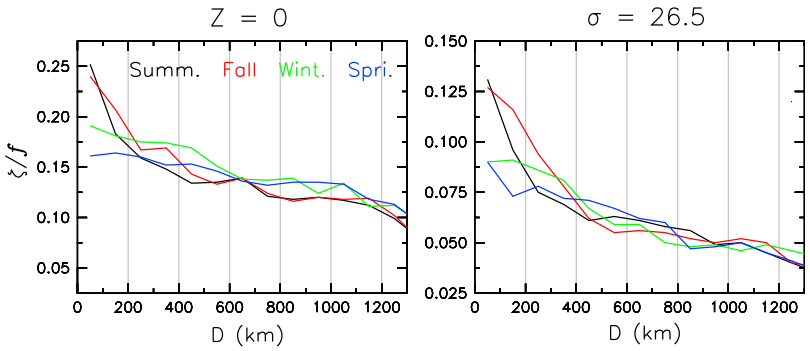

Figure 14. Alongshore-averaged eddy strength $|\zeta/f|$ as a function of the distance from the coast (D) for each season from ROMS.

region with the highest eddy occurrence is seen near the coast, to the north of 40°N at the surface, which is associated with the mesoscale eddies forming due to the offshore separation of the CC at the surface [*Batteen et al.*, 2003]. Westward propagation of these eddies contributes to the elevated eddy occurrence in the offshore region, to the north of 38°N. High eddy occurrence is also noted off Point Conception at the surface. At subsurface, the maximum eddy occurrence is seen all along the coast, which corresponds to the undercurrent eddies.

[42] Eddy polarity shows rather a noisy pattern (Figure 15, right). However, the cyclonic dominance at the surface and the anticyclonic dominance at the subsurface can be clearly identified. Eddy analysis by *Chelton et al.* [2011] has shown that the mesoscale variability is anticyclonic in the nearshore region and cyclonic on the offshore side of the CC. However, such a clear demarcation is not apparent in present analysis, though anticyclonic persistence near the coast is visible to the north of Cape Blanco (~43°N), and between Monterey Bay and Point Conception (~34°N). At $\sigma = 26.5$, the coastal region shows a clear anticyclonic dominance, except in the region between Cape Mendocino (~40°N) and Cape Blanco (~43°N), where cyclonic polarity is persistent at both levels.

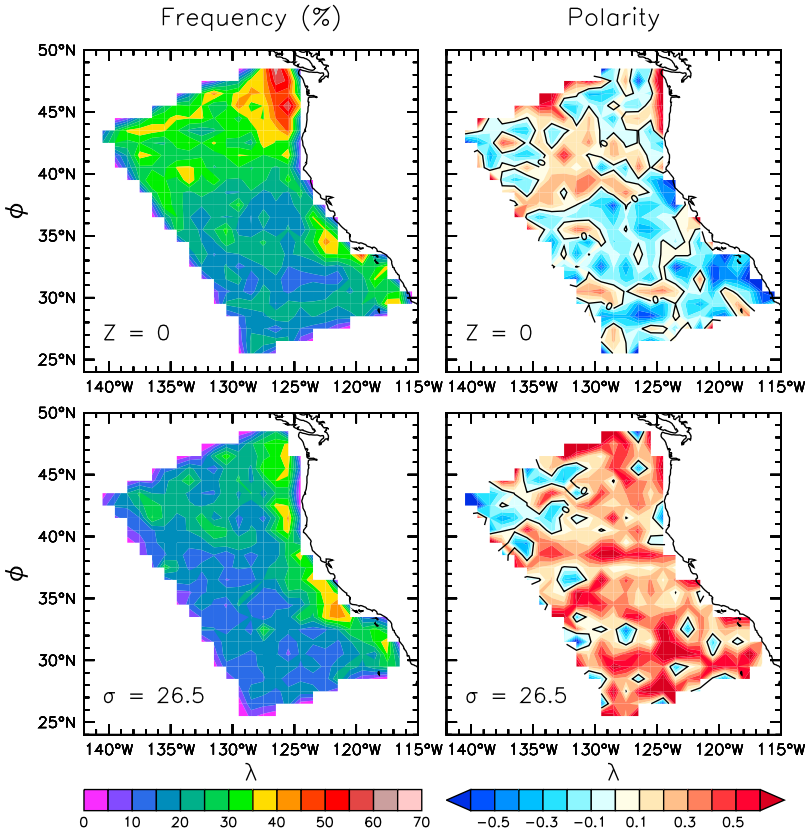

Figure 15. (left) Eddy frequency (percentage of time when at least one eddy is present in a 1° × 1° box) and (right) eddy polarity $((N_a - N_c)/(N_a + N_c)$, where N_a is number of anticyclones and N_c is number of cyclones) for eddies with L ≥ 30 days from ROMS.

5.8. Birth and Death

[43] Eddy birth and death locations are distributed over the entire model domain, although with some spatial patterns. Both at surface and subsurface, for L ≥ 30 days, there are more cyclone birth events close to the coast than offshore. The coastal region to the south of Cape Mendocino (~40°N) shows a high occurrence of cyclone births at the surface, in agreement with the polarity pattern (Figure 15). No such patterns exist for eddies with L ≥ 90 days. Close to the coast, the cyclone birth events show a distinct minimum between northern part of the Southern California Bight (SCB) and the Monterey Bay (between 33°–38°N latitudes) for very long-lived (≥180 days) cases (Figure 10). The high frequency of anticyclone (with L ≥ 30 days) birth at the surface is seen to the north of Cape Blanco (~43°N) and to the south of Point Sur (~36°N), including some parts of the coastal SCB. The birth rate is also elevated in the offshore region to the west of 130°W and to the north of 39°N, consistent with the polarity pattern (Figure 15). There are only a few very long-lived anticyclones formed to the south of Monterey Bay. At the subsurface, only a few very long-lived cyclones form close to the coast, while anticyclones show higher instances of eddy birth close to the coast, irrespective of L. Birth events of subsurface anticyclones are frequent off Point Conception and Cape Mendocino (Figure 10).

[44] Death events are frequent along the near coastal region for both eddy types with L ≥ 30 days at subsurface, with a pronounced peak between Point Arena and the northern part of the SCB (not shown). A high frequency of death events are observed at the surface for the cyclones to the south of Monterey Bay and for anticyclones off Point Conception and to the north of Cape Blanco. Death locations of very long-lived eddies are scattered in the offshore region (Figure 10).

[45] The results of regional birth/death properties should be interpreted with caution as they are highly dependent on the accuracy with which the individual eddies are compiled into tracks. There is the chance for splitting a track into multiple tracks, owing to the weakening or distortion of eddies during their life. This could introduce artificial birth and death instances and reduce or extend the lifetime of the individual tracks.

[46] The composite of eddy properties for the first few weeks after birth and the last few weeks before death displays a systematic evolution for both polarities at both levels (not shown). Within a few days (10–45) after birth, the eddy radius increases by about 7 km, the shape error (section 3.1) decreases sharply by 7.5% (on a scale of 0–35%), and the eddy strength/amplitude (section 3.1) increases slightly. During the last few days before eddy death the size decreases, and the shape error increases with similar magnitudes, but there is a very gradual decrease in eddy amplitude.

5.9. Vertical Structure

[47] To delineate the vertical structure of eddies, we constructed composite maps of eddy anomaly. Eddy anomaly for a field at a given time and depth level is found by removing the horizontal average of the field over a box of 85 km × 85 km, centered around the eddy. This method is more convenient than the "differential anomaly" method [*Simpson et al.*, 1984] commonly used with field observations, as it is tricky to define eddy points and far field points consistently with respect to the large range of eddy sizes found in the CCS. Hence, the anomaly values presented here are probably a lower bound. In addition, the anomaly values will be somewhat dampened with the compositing on fixed depth levels, especially for the subsurface eddies for which the core depth increases as it moves offshore. Only those eddies with L ≥ 90 days are considered for the analysis. There is no horizontal asymmetry in the eddy structure for the fields analyzed and, hence, only the east-west cross section is presented. Since the surface and subsurface cyclones have similar vertical structures, only the surface case is presented for the cyclones. For the σ = 26.5 case, only the undercurrent-generated eddies (eddy birth within 250 km from the coastline) are included in the analysis.

[48] The eddy anomaly composite for ζ/f and temperature (T) are shown in Figure 16. Eddy effects penetrate to depths of about 800–1500 m, with a gradually decreasing horizontal extent toward the bottom (Figure 16). Cyclones have a surface-intensified ζ/f structure, with maximum values of the ζ/f anomaly (0.16) occurring at the surface level. There is a sharp decrease in the ζ/f anomaly within the upper 400 m with the highest values in the upper 200 m as seen in field observations [*Simpson and Lynn*, 1990]. The T anomaly for cyclones also shows a similar structure, with a maximum of −0.78°C at 125 m depth, within the thermocline region [*Simpson and Lynn*, 1990]. The T anomaly for cyclones is confined within the upper 900 m. The similarity in vertical structure between cyclones tracked at surface and subsurface levels clearly illustrates that the cyclones tracked at σ = 26.5 are indeed subsurface expressions of those generated at the surface (section 3.3). Hence, it appears that undercurrent-generated cyclones with a subsurface core are either rare or do not exist.

[49] The vertical structure of ζ/f and the T anomalies for surface anticyclones are similar to the picture depicted above for cyclones, with a maximum ζ/f anomaly occurring at the surface (−0.13 s) and a maximum T anomaly of 0.48°C at 125 m depth. However, anticyclones tracked at σ = 26.5 show a different structure. A maximum value of the ζ/f anomaly (−0.13 s) occurs at 250 m depth, below the thermocline, as seen in observations [*Simpson and Lynn*, 1990]. The horizontal extent of the ζ/f anomaly decreases gradually with depth for anticyclones, versus the rapid decreases for cyclones. High values of the T anomaly also occur below the thermocline, with a maximum value of 0.4°C at 400 m depth. This clearly demonstrates that the ("distinct") anticyclones tracked at σ = 26.5 are formed at subsurface, below the thermocline. This T anomaly structure compares very well with the observations by *Simpson et al.* [1984, Figure 11] with two exceptions: the model T anomaly is weaker and there is no negative T anomaly above the eddy core (created by upward doming of isotherms). In fact, this particular eddy observed by *Simpson et al.* [1984] had an anomalously high T at its core, as later discussed by *Simpson and Lynn* [1990]. The negative T anomaly above the core of the subsurface anticyclones is not always seen in the observations [*Simpson and Lynn*, 1990; *Jerónimo and Gómez-Valdés*, 2007], and in the model it is limited to occasions where the eddy is well isolated from its surroundings. Downwelling and the equatorial origin of warm undercurrent waters contributes to the high subsurface T anomaly.

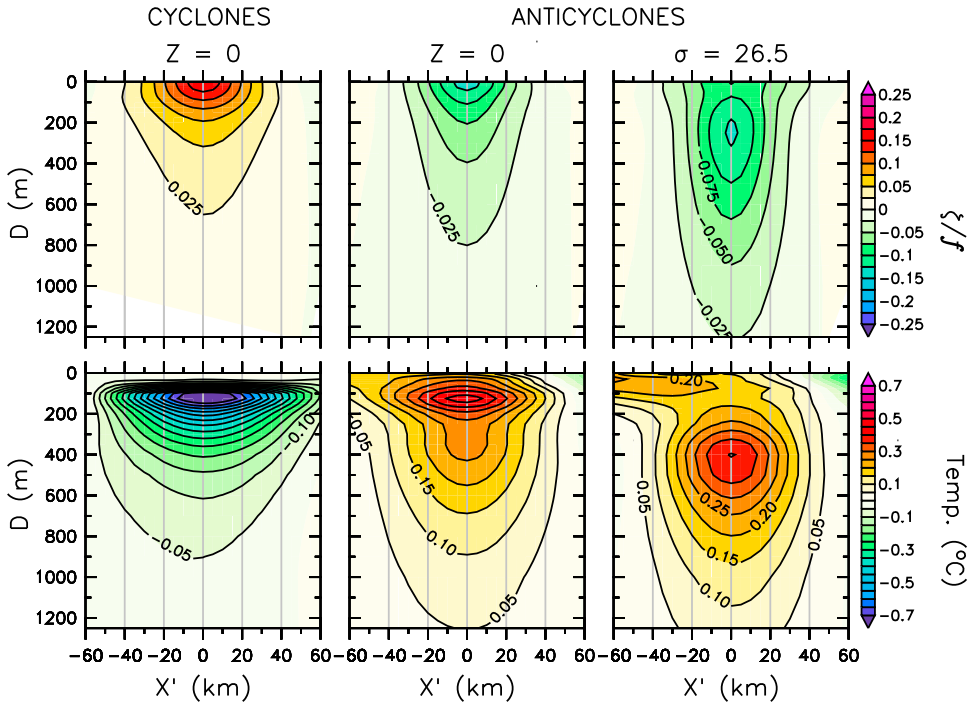

Figure 16. Composite anomaly (relative to the horizontal mean of the 85 km × 85 km box, relative to the eddy center) for eddies with lifetime L ≥ 90 day from ROMS: (top) vorticity ζ/f and (bottom) temperature (°C). D is depth (m) and X′ is the east (positive) and west (negative) distance relative to the eddy center (km). For the σ = 26.5 case, only eddies generated within 250 km from the coast are included.

[50] We also analyzed the salinity (S) anomaly composites for both surface and subsurface tracked anticyclones (Figure 17) to study their water mass properties. Anticyclones at the surface show a fresh anomaly within the upper 300 m, with a maximum of −0.07 practical salinity units (psu) around the 50 m depth. This is consistent with the downwelling within the anticyclone, which push the relatively fresher water at the surface to deeper depths. Anticyclones tracked at the subsurface show a well defined positive S anomaly between 100–600 m, with two maxima of 0.031 psu at 150 m and 0.032 psu at 400 m. This positive anomaly, although weak, clearly shows that these eddies have their origin in the undercurrent. In the composite of the actual S field, the eddy core is only visible as a general doming of isohalines (not shown). This is because the undercurrent waters mix with surrounding water during their journey. [*Reed and Halpern*, 1976] and hence the undercurrent-generated eddies do not always have a well defined S signature [*Cornuelle et al.*, 2000]. In addition, the high gradients of S over the CCS domain considered here make the S signatures less visible in the composites. A similar analysis of the Chile Undercurrent–generated anticyclones (in the latitude band 26°S–34°S, from model solution) show a well defined blob of high-S water between 100–600 m, with its core at 250 m (F. Colas et al., Heat balance and eddies in the Peru-Chile current system, submitted to *Climate Dynamics*, 2011). A more recent study using Argo profiling floats in the eastern south Pacific also shows similar salinity structure for undercurrent generated anticyclones (A. Chaigneau et al., Vertical structure of mesoscale eddies in the eastern South Pacific ocean: A composite analysis from altimetry and Argo profiling floats, manuscript in preparation, 2011). The high-S core of the undercurrent off Chile is well distinguishable with low-S water above and below it. However, such a clear pattern does not exist off California. The fresh S anomaly seen at the surface (0–50 m) for the σ = 26.5 anticyclones is brought in by the downwelling associated with the anticyclonic circulation in the surface layer, which pushes down the relatively fresh surface waters. There is no subsurface (below 200 m) salinity anomaly associated with cyclones tracked at σ = 26.5 (not shown). The difference in vertical structure (in ζ/f,

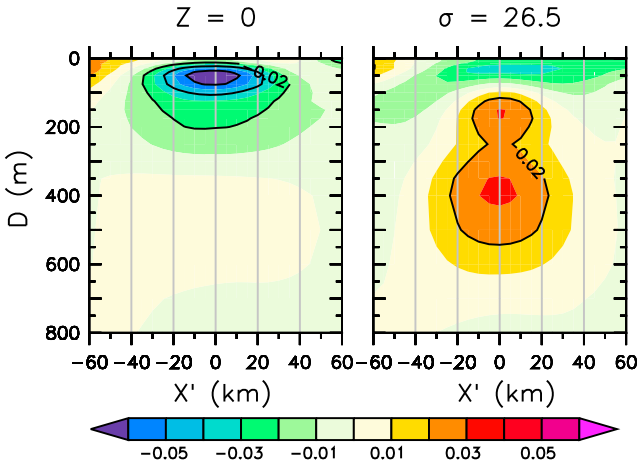

Figure 17. As in Figure 16, but for the salinity (psu) of anticyclones.

temperature, and salinity) between anticyclones tracked at $z = 0$ and $\sigma = 26.5$ levels implies that they are clearly distinguishable in their vertical structure and there are distinct generation processes at both levels.

6. Summary

[51] Eddy properties in the CCS are studied with a high-resolution ($dx = 5$ km) climatological regional model solution and an altimetry analysis, using eddy tracking algorithms. Eddy identification is made using a closed contour method on the SSH anomaly field (SSH method) and velocity-gradient parameter (Q method). With the eddy identification and tracking tool, special care is taken to identify all possible eddies that are nearly circular in shape, that have a radius within an appropriate range, and that have a minimum amplitude for the SSH anomaly or ζ/f. Eddies are tracked in successive snapshots by comparing their position and change in properties, making sure that most suitable eddies are joined together to form an eddy track. A comparison of eddy properties between the model and altimetry, using the SSH method, shows remarkable uniformity with respect to space and time and even in polarity to a lesser extent in the CCS region. However, weaker model currents lead to strong meridional deflection of eddies in the model.

[52] The major properties of the CCS eddies from the model eddy analysis are the following: there is cyclonic dominance in the long-lived eddies formed at surface in the CCS and anticyclonic dominance in the undercurrent-generated eddies at the subsurface. Anticyclones form both at the surface and subsurface, whereas no long-lived cyclones with a subsurface core are seen to be generated from the undercurrent. Other than the ζ/f amplitude measure (stronger for surface eddies (0–0.5) and weaker for subsurface eddies (0–0.25), section 5.1) and nonlinearity (surface eddies are strongly nonlinear, section 5.4), there is no significant difference between surface and subsurface eddies in terms of size (15–70 km) and no significant difference in westward propagation speeds (peaks at 1–2 km/day). There is remarkable uniformity between eddy polarities in radius, nonlinearity, and westward propagation speed. Only the near-coastal subsurface-generated eddies show a prominent seasonal cycle in eddy birth. Whereas, eddy energy and amplitude levels show a clear seasonal cycle with the maximum near the coast during summer, offshore migration during the fall and winter, and a minimum during spring (section 5.6). At the surface eddy activity is high near the coast, with a well defined maximum to the north of Cape Blanco (~43°N) and in the offshore region to the north of 38°N (section 5.7). Subsurface eddies are frequent near the coastal region, but less frequent offshore. Along the coast there are a few key areas where eddy formation is frequent (e.g., off Cape Mendocino, off Point Conception, and to the north of Cape Blanco), and there are regions where birth events are rare (e.g., between the northern SCB and Monterey Bay), but it depends on eddy polarity and whether they are formed at surface or subsurface. There are regional preferences for eddy polarity to the south of 38°N, with cyclonic dominance at surface and anticyclonic dominance at subsurface. Eddy properties like radius, shape error, and strength show a consistent pattern of change during the few weeks following the eddy birth (radius increases, the shape error decreases, and the strength increases) and the few weeks before the eddy death (radius decreases, shape error increases, and strength decreases) (section 5.8).

[53] The analysis of model eddies show that eddy signals penetrate to 800–1500 m in depth. Cyclones tracked at both levels and anticyclones tracked at the surface have a surface-intensified structure, with a maximum ζ/f anomaly at the surface level and a maximum temperature anomaly around 100–125 m depth, within the thermocline. In general, cyclones have stronger ζ/f and temperature anomalies. However, no long-lived cyclones with a subsurface vorticity core or subsurface salinity anomaly are identified in this study. Hence, cyclones tracked at the $\sigma = 26.5$ level are indeed vertical extensions of cyclones generated at the surface. Subsurface anticyclones show a strikingly different structure, with a maximum ζ/f anomaly at 250 m depth and maximum temperature anomaly at 400 m depth. Surface anticyclones have fresh salinity anomalies associated with downwelling at the surface. Subsurface anticyclones show clearly a subsurface positive anomaly in salinity, though not very strong. The subsurface core of subsurface anticyclones and the salinity anomaly confirm their formation in the undercurrent.

[54] The ability to identify and track eddies in space and time opens up many new possibilities in the study of mesoscale eddies, in the context of CCS and other similar eddy active regions, too. In the present study we address only the general properties (e.g., radius, shape, lifetime, abundance, strength, westward propagation characteristics, nonlinearity, seasonal cycle, birth and death, and vertical structure) of the CCS eddies, focusing on eddies with lifetimes over a month and/or a season. Many aspects of the CCS eddies have yet to be explored. For example, with space-time information about eddies, estimates of offshore heat and mass transport by mesoscale eddies can be made more precisely. A study in this direction by *Treguier et al.* [2003], shows that transport estimates by Agulhas rings using a conventional method (perturbation to the time-mean flow) and by an eddy method (based on the water trapped inside the eddy) show significant differences, with the latter always being higher. It is also interesting to study the short-lived ($L < 30$ days) eddies exclusively: there are many of them forming near the coast and propagating offshore. Even though their lifespan is short, they could play an important role in material transport and even in the mixing to an extent, within the near-coastal region. Near-coastal standing eddies [*Marchesiello et al.*, 2003] also need special attention. The role of mesoscale eddies in various biological processes in the CCS, like injection of nutrients into the euphotic zone and offshore transport of biogenic material, can be better addressed with physics-biology coupled models and eddy tracking tools. The CCS region is known to exhibit strong interannual variability (e.g., El Niño–Southern Oscillation) and hence is expected to have a signature in eddy activity, too.

Appendix A: Different Measures of Eddy Strength and Size

[55] The different eddy detection methods in section 3 are based on different fields. Here we illustrate how the strength and size measures are expected to differ with the field

choice. We assume that a typical horizontal eddy shape is an axisymmetric Gaussian in dynamic height or sea level anomaly,

$$\eta = \eta_0 e^{-(r/r_0)^2}, \tag{A1}$$

where r is radial distance from the center. If the eddy is geostrophic, then related fields are

$$\begin{aligned} v &= -\frac{2g\eta_0}{fr_0^2}\, r\, e^{-(r/r_0)^2} \\ \zeta &= -\frac{4g\eta_0}{fr_0^2}\left[1-\left(\frac{r}{r_0}\right)^2\right] e^{-(r/r_0)^2} \\ Q &= \left(\frac{2g\eta_0}{fr_0^2}\right)^2\left[1-2\left(\frac{r}{r_0}\right)^2\right] e^{-2(r/r_0)^2}. \end{aligned} \tag{A2}$$

[56] For eddy strength in the SSH method, we choose an outer fractional contour value of C_0 (*e.g.*, $C_0 = 0.2$), hence the strength is $(1 - C_0)\eta_0$ (*e.g.*, $0.8\eta_0$). For the Q method the strength is $4g\eta_0/f^2r_0^2$.

[57] For eddy size with the SSH method, $R = \sqrt{-\ln[C_0]}\,r_0$ (*e.g.*, $1.27r_0$). With our Q method using the distance to $\zeta = 0$, $R = r_0$. If instead we measured size by the distance to $Q = 0$, R would be $r_0/\sqrt{2}$; this is the same size as the location of the maximum in v.

[58] However, since not all eddies have exactly the same shape, these comparative strength and size measures will differ somewhat for particular eddies.

[59] **Acknowledgments.** The altimeter products were produced by Ssalto/Duacs and distributed by AVISO, with support from CNES (http://www.aviso.oceanobs.com/duacs/). We appreciate the support of the Office of Naval Research through the grants N00014-08-1-0597 and N00014-10-1-0484. D.B.C.'s contribution to this research was funded as part of the NASA Ocean Surface Topography Science Team through NASA grant NNX08AR37G.

References

Batteen, M. L., N. J. Cipriano, and J. T. Monroe (2003), A large-scale seasonal modeling study of the California Current System, *J. Oceanogr.*, *59*, 545–562.

Beron-Vera, F. J., M. J. Olascoaga, and G. J. Goni (2008), Oceanic mesoscale eddies as revealed by Lagrangian coherent structures, *Geophys. Res. Lett.*, *35*, L12603, doi:10.1029/2008GL033957.

Brink, K. H., R. C. Beardsley, J. Paduan, R. Limeburner, M. Caruso, and J. G. Sires (2000), A view of the 1993–1994 California Current based on surface drifters, floats, and remotely sensed data, *J. Geophys. Res.*, *105*(C4), 8575–8604.

Capet, X., F. Colas, J. C. McWilliams, P. Penven, and P. Marchesiello (2008), Eddies in eastern-boundary subtropical upwelling systems, in *Ocean Modeling in an Eddying Regime*, *Geophys. Monogr. Ser.*, vol. 177, edited by M. Hecht and H. Hasumi, pp. 131–148, AGU, Washington, D. C.

Carton, J., and B. Giese (2008), A reanalysis of ocean climate using Simple Ocean Data Assimilation (SODA), *Mon. Weather Rev.*, *136*(8), 2999–3017.

Chaigneau, A., G. Eldin, and B. Dewitte (2009), Eddy activity in the four major upwelling systems from satellite altimetry (1992–2007), *Prog. Oceanogr.*, *83*, 117–123.

Chelton, D. B. (1984), Seasonal variability of alongshore geostrophic velocity off central California, *J. Geophys. Res.*, *89*(C3), 3473–3486.

Chelton, D. B., M. G. Schlax, R. M. Samelson, and R. A. de Szoeke (2007), Global observations of large oceanic eddies, *Geophys. Res. Lett.*, *34*, L15606, doi:10.1029/2007GL030812.

Chelton, D. B., M. G. Schlax, and R. M. Samelson (2011), Global observations of nonlinear mesoscale eddies, *Prog. Oceanogr.*, in press.

Chereskin, T. K., M. Y. Morris, P. P. Niiler, P. M. Kosro, R. L. Smith, S. R. Ramp, C. A. Collins, and D. L. Musgrave (2000), Spatial and temporal characteristics of the mesoscale circulation of the California Current from eddy resolving moored and shipboard measurements, *J. Geophys. Res.*, *105*(C1), 1245–1269.

Collins, C. A., N. Garfield, T. A. Rago, F. W. Rischmiller, and E. Carter (2000), Mean structure of the inshore countercurrent and California Undercurrent off Point Sur, California, *Deep Sea Res., Part II*, *47*, 765–782.

Collins, C. A., L. M. Ivanov, and O. V. Melnichenko (2003), Seasonal variability of the California undercurrent: Statistical analysis based on the trajectories of floats with neutral buoyancy, *J. Phys. Oceanogr.*, *13*(3), 135–147.

Cornuelle, B. D., T. K. Chereskin, P. P. Niiler, and M. Y. Morris (2000), Observations and modeling of a California undercurrent eddy, *J. Geophys. Res.*, *105*(C1), 1227–1243.

Cushman-Roisin, B. (1994), *Introduction to Geophysical Fluid Dynamics*, 320 pp., Prentice Hall, Englewood Cliffs, N. J.

da Silva, A. M., C. C. Young-Molling, and S. Levitus (1994), *Atlas of Surface Marine Data* 1994, vol. 1, *Algorithms and Procedures*, 83 pp., U.S. Dep. of Commer., Washington, D. C.

Doglioli, A. M., B. Blanke, S. Speich, and G. Lapeyre (2007), Tracking coherent structures in a regional ocean model with wavelet analysis: Application to Cape Basin eddies, *J. Geophys. Res.*, *112*, C05043, doi:10.1029/2006JC003952.

Flierl, G. R., and J. C. McWilliams (1977), On the sampling requirements for measuring moments of eddy variability, *J. Mar. Res.*, *35*, 797–820.

Garfield, N., C. A. Collins, R. G. Paquette, and E. Carter (1999), Lagrangian exploration of the California undercurrent, 1992–95, *J. Phys. Oceanogr.*, *29*(4), 560–583.

Haidvogel, D. B., et al. (2009), Ocean forecasting in terrain-following coordinates: Formulation and skill assessment of the regional ocean modelling system, *J. Comp. Phys.*, *227*, 3595–3624. [Correction, *J. Comp. Phys.*, *228*, 8985, 2009.]

Henson, S. A., and A. C. Thomas (2008), A census of oceanic anticyclonic eddies in the Gulf of Alaska, *Deep Sea Res., Part I*, *55*, 163–176.

Hickey, B. M. (1979), The California Current System—Hypothesis and facts, *Prog. Oceanogr.*, *12*, 259–284.

Hickey, B. M. (1998), Coastal oceanography of western North America from the tip of Baja California to Vancouver Island: Coastal segment, in *The Sea*, vol. 11, *The Global Coastal Ocean: Regional Studies and Syntheses*, edited by A. R. Robinson and K. H. Brink, pp. 345–391, John Wiley, Hoboken, N. J.

Huyer, A., J. A. Barth, P. M. Kosro, R. K. Shearman, and R. L. Smith (1998), Upper-ocean water mass characteristics of the California Current, summer 1993, *Deep Sea Res., Part II*, *45*, 1411–1442.

Isern-Fontanet, J., E. García-Ladona, and J. Font (2003), Identification of marine eddies from altimetric maps, *J. Atmos. Oceanic Technol.*, *20*(5), 772–778.

Isern-Fontanet, J., J. Font, E. García-Ladona, M. Emelianov, C. Millot, and I. Taupier-Letage (2004), Spatial structure of anticyclonic eddies in the Algerian Basin (Mediterranean Sea) analyzed using the Okubo-Weiss parameter, *Deep Sea Res., Part II*, *51*, 3009–3028.

Jerónimo, G., and J. Gómez-Valdés (2007), A subsurface warm-eddy off northern Baja California in July 2004, *Geophys. Res. Lett.*, *34*, L06610, doi:10.1029/2006GL028851.

Kelly, K. A., R. C. Beardsley, R. Limeburner, and K. H. Brink (1998), Variability of the near-surface eddy kinetic energy in the California Current based on altimetric, drifter and moored current data, *J. Geophys. Res.*, *103*(C6), 13,067–13,083.

Logerwell, E. A., and P. E. Smith (2001), Mesoscale eddies and survival of late stage Pacific sardine (*Sardinops sagax*) larvae, *Fish. Oceanogr.*, *10*(1), 13–25, doi:10.1111/j.1365-2419.2001.00152.x.

Lukas, R., and F. Santiago-Mandujano (2001), Extreme water mass anomaly observed in the Hawaii ocean time-series, *Geophys. Res. Lett.*, *28*(15), 2931–2934.

Lumpkin, R., and Z. Garraffo (2005), Evaluating the decomposition of tropical Atlantic drifter observations, *J. Atmos. Oceanic Technol.*, *22*(9), 1403–1415.

Luo, J., and L. Jameson (2002), A wavelet-based technique for identifying, labeling and tracking of ocean eddies, *J. Atmos. Oceanic Technol.*, *19*(3), 381–390.

Lynn, R. J., and J. J. Simpson (1987), The California Current System: The seasonal variability of its physical characteristics, *J. Geophys. Res.*, *92*(C12), 12,947–12,966.

Mantyla, A. W., S. J. Bograd, and E. L. Venrick (2008), Patterns and controls of chlorophyll-*a* and primary productivity cycles in the Southern California Bight, *J. Mar. Syst.*, *73*, 48–60, doi:10.1016/j.jmarsys.2007.08.001.

Marchesiello, P., J. C. McWilliams, and A. Shchepetkin (2001), Open boundary conditions for long-term integration of regional oceanic models, *Ocean Modell.*, *3*, 1–20.

Marchesiello, P., J. C. McWilliams, and A. Shchepetkin (2003), Equilibrium structure and dynamics of the California Current System, *J. Phys. Oceanogr.*, *33*, 753–783.

McWilliams, J. C. (1999), The vortices of homogeneous geostrophic turbulence, *J. Fluid Mech.*, *401*, 1–26.

McWilliams, J. C., and G. R. Flierl (1979), On the evolution of isolated nonlinear vortices, *J. Phys. Oceanogr.*, *9*, 1155–1182.

Morrow, R., F. Birol, D. Griffin, and J. Sudre (2004), Divergent pathways of cyclonic and anti-cyclonic ocean eddies, *Geophys. Res. Lett.*, *31*, L24311, doi:10.1029/2004GL020974.

Nencioli, F., C. Dong, T. Dickey, L. Washburn, and J. C. McWilliams (2010), A vector geometry based eddy detection algorithm and its application to a high-resolution numerical model product and high-frequency radar surface velocities in the Southern California Bight, *J. Atmos. Oceanic Technol.*, *27*(3), 564–579.

Okubo, A. (1970), Horizontal dispersion of floatable particles in the vicinity of velocity singularities such as convergences, *Deep Sea Res. Oceanogr. Abstr.*, *17*, 445–454.

Palacios, D. M., and S. J. Bograd (2005), A census of Tehuantepec and Papagayo eddies in the northeastern tropical Pacific, *Geophys. Res. Lett.*, *32*, L23606, doi:10.1029/2005GL024324.

Pares-Sierra, A., W. B. White, and C. Tai (1993), Wind-driven coastal generation of annual mesoscale eddy activity in the California Current, *J. Phys. Oceanogr.*, *23*(6), 1110–1121.

Pascual, A., Y. Faugere, G. Larnicol, and P. Le Traon (2006), Improved description of the ocean mesoscale variability by combining four satellite altimeters, *Geophys. Res. Lett.*, *33*, L02611, doi:10.1029/2005GL024633.

Pierce, S. D., R. L. Smith, P. M. Kosro, J. A. Barth, and C. D. Wilson (2000), Continuity of the poleward undercurrent along the eastern boundary of the mid-latitude north Pacific, *Deep Sea Res., Part II*, *47*, 811–829.

Reed, R. K., and D. Halpern (1976), Observation of the California Undercurrent off Washington and Vancouver Island, *Limnol. Oceanogr., 21*(3), 389–398.

Sadarjoen, I. A., F. H. Post, B. Ma, and D. C. Banks (1998), Selective visualization of vortices in hydrodynamic flows, in *Visualization '98: Proceedings, October 18–23, 1998, Research Triangle Park, North Carolina*, pp. 419–422, ACM Press, New York.

Samelson, R. M., and S. Wiggins (2006), *Lagrangian Transport in Geophysical Jets and Waves: The Dynamical Systems Approach*, 147 pp., Springer, New York.

Sangrà, P., et al. (2009), The Canary Eddy Corridor: A major pathway for long-lived eddies in the subtropical north Atlantic, *Deep Sea Res., Part I*, *56*, 2100–2114.

Shchepetkin, A., and J. C. McWilliams (2005), The regional oceanic modeling system (ROMS): A split-explicit, free-surface, topography-following-coordinate ocean model, *Ocean Modell.*, *9*, 347–404.

Shearman, R. K., J. A. Barth, and P. M. Kosro (1999), Diagnosis of the three-dimensional circulation associated with mesoscale motion in the California Current, *J. Phys. Oceanogr.*, *29*, 651–670.

Simpson, J. J., and R. J. Lynn (1990), A mesoscale eddy dipole in the offshore California Current, *J. Geophys. Res.*, *95*(C8), 13,009–13,022.

Simpson, J. J., T. D. Dickey, and C. J. Koblinsky (1984), An offshore eddy in the California Current System Part I: Interior dynamics, *Prog. Oceanogr.*, *13*, 5–49.

Sipp, D., E. Lauga, and L. Jacquin (1999), Vortices in rotating systems: Centrifugal, elliptic, and hyperbolic type instabilities, *Phys. Fluids*, *11*(12), 3716–3728.

Stegmann, P. M., and F. Schwing (2007), Demographics of mesoscale eddies in the California Current, *Geophys. Res. Lett.*, *34*, L14602, doi:10.1029/2007GL029504.

Strub, P. T., and C. James (2000), Altimeter-derived variability of surface velocities in the California Current System: 2. Seasonal circulation and eddy statistics, *Deep Sea Res., Part II*, *47*, 831–870.

Treguier, A. M., O. Boeber, B. Barnier, and G. Madec (2003), Agulhas eddy fluxes in a 1/6° Atlantic model, *Deep Sea Res., Part II*, *50*, 251–280.

Weiss, J. (1991), The dynamics of enstrophy transfer in two dimensional hydrodynamics, *Physica D*, *48*(2–3), 273–294.

X. Capet, Laboratoire de Physique des Océans, UMR 6523, CNRS-IFREMER-UBO, Plouzane F-29280, France.

D. B. Chelton, College of Oceanic and Atmospheric Sciences, Oregon State University, Corvallis, OR 97331, USA.

F. Colas, J. Kurian, and J. C. McWilliams, Institute of Geophysics and Planetary Physics, University of California, Los Angeles, CA 90095-1567, USA. (jaison@atmos.ucla.edu)